

Optical signatures of lightning-induced electron precipitation

R. A. Marshall,^{1,2} J. Bortnik,³ N. Lehtinen,⁴ and S. Chakrabarti¹

Received 7 April 2011; revised 4 May 2011; accepted 13 May 2011; published 10 August 2011.

[1] Model calculations are conducted to estimate the optical emission brightness caused by lightning-induced electron precipitation. Pitch angle scattering of energetic radiation belt electrons by lightning-generated whistler mode waves results in precipitation in the upper atmosphere. Assuming a lightning peak current and location, plasmasphere distribution, and radiation belt density and pitch angle distributions, we calculate the secondary ionization production and optical emissions in a number of lines and bands. We find that the brightness in N₂ 1P and O(¹S) may reach a few to 10 R for a 100 kA peak current discharge, with a distinct spatial and temporal signature of 1–2 s. A simple signal-to-noise ratio (SNR) calculation shows that this signature should be detectable with modern photometric instruments with an SNR ~4. We further investigate the dependence of this brightness on lightning source latitude and peak current.

Citation: Marshall, R. A., J. Bortnik, N. Lehtinen, and S. Chakrabarti (2011), Optical signatures of lightning-induced electron precipitation, *J. Geophys. Res.*, 116, A08214, doi:10.1029/2011JA016728.

1. Introduction

[2] Intense lightning discharges emit an electromagnetic pulse (EMP) in the VLF frequency range, the intensity of which may reach 50 V/m at 100 km range [e.g., *Rakov and Uman*, 2003]. Most of the EMP energy propagates in the Earth-ionosphere waveguide, but a fraction leaks through the lossy ionosphere and propagates as whistler mode waves in the magnetosphere. In the course of their propagation, these waves will interact in cyclotron resonance with relativistic radiation belt electrons, resulting in pitch angle scattering of these electrons [e.g., *Voss et al.*, 1984]. A small fraction of these electrons will be scattered into the bounce- or drift-loss cones, whereupon they will be precipitated in the upper atmosphere during their subsequent bounce or drift period.

[3] Secondary ionization formed by this precipitation has been detected for decades using subionospheric VLF remote sensing; such events are known as Trimpi or lightning-induced electron precipitation (LEP) events [*Helliwell*, 1965; *Inan et al.*, 2010]. This detection method has been used to show that LEP events are commonly associated with obliquely propagating (rather than ducted) whistlers [*Johnson et al.*, 1999] and have constrained the spatial precipitation region and time signature [*Johnson et al.*, 1999; *Lauben et al.*, 1999]. *Peter and Inan* [2007] used LEP observations to estimate the total precipitated flux of

$\sim 10^{-2}$ ergs/cm²/s, due to a 133 kA discharge in northwest Texas. However, the VLF subionospheric method is unable to resolve the precipitated electron energy spectra or altitude profiles. LEP events have also been observed on satellites, perhaps most famously reported by *Voss et al.* [1984, 1998]. Therein, an LEP burst of 10⁻³ ergs/cm²/s was reported in the region $2 < L < 3$. This L shell range coincides with the slot region, and at slightly higher or lower L shells, the available radiation belt flux increases considerably.

[4] In addition to secondary ionization, lightning-induced electron precipitation will also result in optical emissions, like aurora. In this paper we estimate the brightness of those emissions to ascertain their detectability from the ground. Detection of optical emissions at multiple wavelengths, combined with the model described herein, could lead to estimates of both altitude profiles of new ionization and precipitated electron energy spectra. In addition, measurement of these signatures will aid in quantifying lightning as a radiation belt loss process. Detection during different phases of geomagnetic storms may also provide estimates of relativistic particle lifetimes during geomagnetic storms. Immediately following storm onset, an enhancement of energetic particles is expected in the slot region [e.g., *Baker et al.*, 2004; *Thorne et al.*, 2007]. Since LEP precipitation peaks in the slot region, these events become more easily observable during storm times [*Peter et al.*, 2006]. As the geomagnetic storm recovers, we expect to see the slot region particle fluxes near the loss cone disappear over the course of 3–5 days [*Baker et al.*, 2004; *Meredith et al.*, 2009], and the optical signatures of LEP events modeled here will become less detectable. In this way it will be possible to measure the lifetimes of these particles by ground-based optical measurements.

2. Model Description

[5] The modeling method used in the present study is described in detail by *Marshall et al.* [2010], and so only an

¹Center for Space Physics, Boston University, Boston, Massachusetts, USA.

²Now at STAR Laboratory, Stanford University, Stanford, California, USA.

³Department of Atmospheric and Oceanic Sciences, University of California, Los Angeles, California, USA.

⁴STAR Laboratory, Stanford University, Stanford, California, USA.

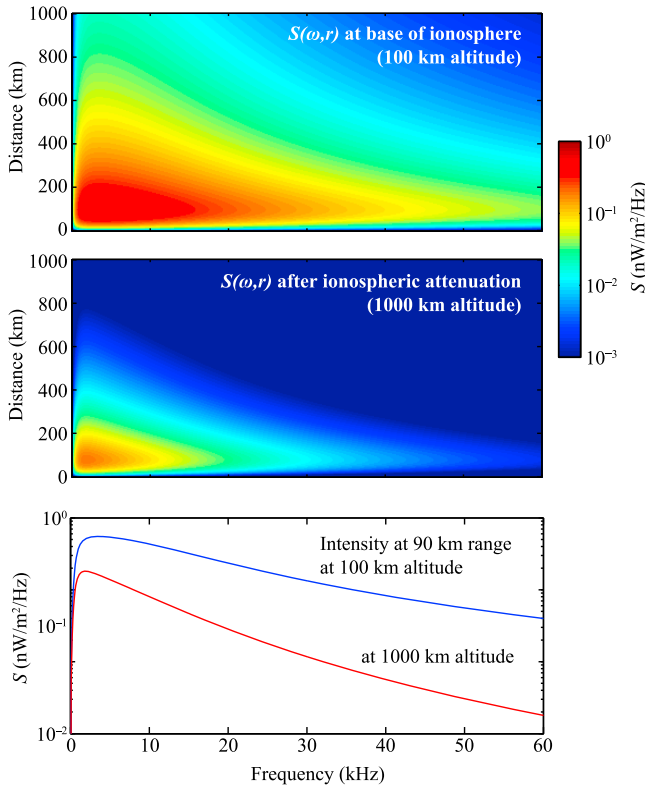


Figure 1. Lightning field intensity as a function of frequency and distance from the source. (top) Intensity at the base of the ionosphere. (middle) Intensity after accounting for attenuation through the ionosphere, using *Helliwell* [1965]. (bottom) Slices of the spectra at 90 km distance.

overview is given below. Our modeling effort primarily utilizes two established models. The first part follows the methodology of *Bortnik et al.* [2006a, and references therein]. The lightning energy is assumed to be confined to the first 20 ms, and is distributed into 130 frequency bins to form a spectrum. The field spectral intensity is then calculated at the base of the ionosphere according to *Bortnik* [2004]:

$$S(\omega) = \frac{1}{Z_0} \left(\frac{\mu_0 h_e I_0}{2\pi} \right)^2 \left(\frac{\sin \kappa}{R} \right)^2 \frac{\omega^2 (a-b)^2}{(\omega^2 + a^2)(\omega^2 + b^2)} \quad (1)$$

where $Z_0 = \sqrt{\mu_0/\epsilon_0} = 377 \Omega$, $h_e = 5$ km is the height of the cloud, I_0 is the lightning peak current in Amperes, κ and R are the zenith angle and distance to a location at the base of the ionosphere, and a and b are equal to 5×10^3 and 10^5 respectively. $S(\omega)$ is in units of $\text{W m}^{-2} \text{Hz}^{-1}$. The wave intensity at 100 km altitude is shown as a function of frequency and radial distance from the lightning source in Figure 1. The spectrum used here peaks at ~ 3.5 kHz, consistent with a lightning discharge of about 300 μs duration. In the time domain, this 100 kA lightning discharge produces a peak electric field of 0.65 V/m at 100 km altitude, about 90 km radial distance from the source.

[6] These fields are then propagated through the ionosphere to 1000 km altitude using an attenuation factor from *Helliwell* [1965, Figure 3–35], as shown in Figure 1 (middle). From there, whistler mode waves are ray traced

through the plasmasphere using the 2D Stanford ray tracer [*Inan and Bell*, 1977], including magnetospheric reflections and path-integrated Landau damping. Wave-particle interactions and scattering near the loss cone are calculated following the method of *Bell* [1984] but using fully relativistic equations and multiple harmonic resonances. This series of calculations results in an estimate of the precipitated flux as a function of time (at 0.2 s resolution), latitude, and electron energy, for each frequency component in the lightning spectrum. This sequence is described in more detail by *Bortnik* [2004].

[7] The second part of the modeling effort uses the Monte Carlo deposition model of *Lehtinen et al.* [2001]. With an input precipitation flux as a function of energy at a given time and latitude, the Monte Carlo model propagates electrons into the upper atmosphere and calculates the energy deposition as a function of altitude, with 1 km altitude resolution. This process is repeated for all time steps and latitudes, and the results are extended in longitude by a scaling factor [*Bortnik*, 2004, equation 5.5], yielding a three-dimensional volume of energy deposition, evolving in time. The Monte Carlo model also calculates the fraction of electrons that are scattered back into the magnetosphere; those electrons will continue to bounce back and forth along their field line, and a fraction will be precipitated on each subsequent bounce, with 1–2 s between each bounce (depending on L shell). However, we do not consider the fate of those backscattered electrons in this work. *Voss et al.* [1998] show that LEP events observed on the S81-1 satellite exhibit multiple peaks, attributed to these repeatedly scattered electrons, and each successive peak is 3–4 times smaller than the previous one. Hence, we would expect to see a similar effect in the optical signature.

[8] Next, we use the well-known result that each 35 eV of deposited energy produces an ionization pair [*Rees*, 1963] to calculate pair production at each point in 3D space. We use the excitation calculation methods of *Vallance Jones* [1974, section 4.2] to find ionization and optical emission rates at each time step in the 3D volume. The equations for the excitation rates for the emissions of interest are given by *Marshall et al.* [2010] and include quenching and cascading effects. Finally, a geometric line-of-sight calculation through the emitting volume yields the emission brightness, in rayleighs, observed at a predetermined location on the ground.

[9] The radiation belt fluxes, plasmasphere density, pitch angle distributions, and atmospheric density models used here are identical to those in Figures 1 and 2 of *Marshall et al.* [2010]. In that previous paper we established that the pitch angle distribution has a very strong effect on the precipitated flux, since the changes in pitch angle due to resonant scattering are very small. Between the square and sine pitch angle distributions shown therein, the resulting precipitated flux, and in turn the ionization and optical emissions, decrease by almost two orders of magnitude. In the present study all of the simulations use the square pitch angle distribution, and we discuss the effects of this choice later.

3. Precipitation, Ionization, and Emission Profiles

[10] The ray tracing and particle precipitation calculations are identical to those conducted and reported by *Bortnik*

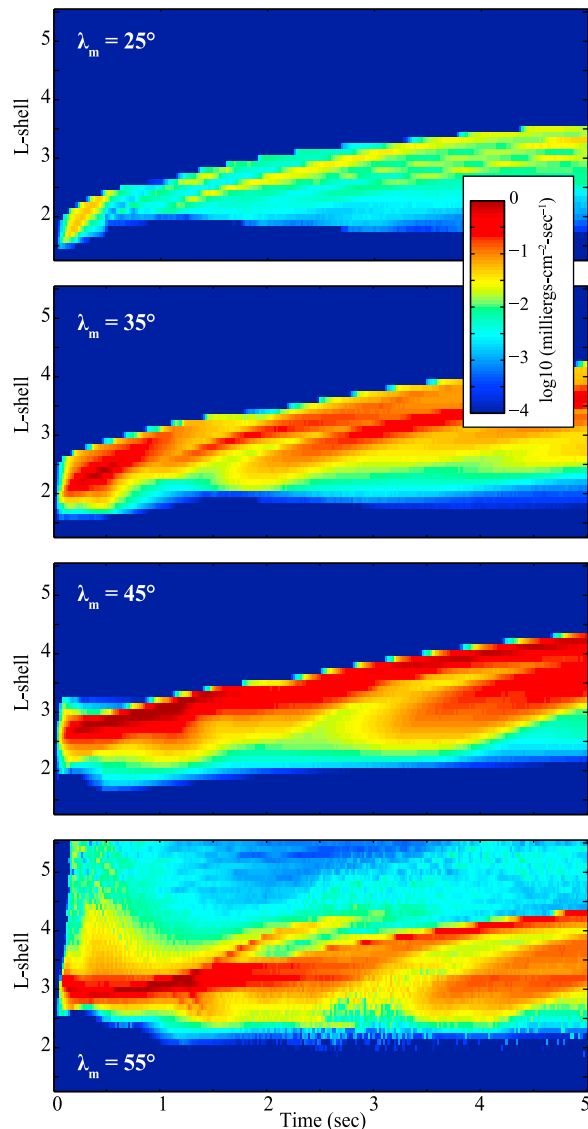


Figure 2. Precipitated flux due to a 100 kA discharge at the magnetic latitudes shown; flux is in units of milliergs $\text{cm}^{-2} \text{s}^{-1}$.

[2004] and *Bortnik et al.* [2006b], except for the lightning peak current and pitch angle distribution. Similar to *Bortnik*, we model lightning sources at geomagnetic latitudes of $\lambda_m = 25^\circ, 35^\circ, 45^\circ$, and 55° . The precipitated fluxes for each of these sources, with 100 kA peak current, are shown in Figure 2. As mentioned in section 2, the use of a square pitch angle distribution increases the magnitude of the precipitated flux by about two orders of magnitude, and the precipitated flux increases linearly with the lightning peak current; otherwise, our results reflect those from *Bortnik* [2004]. These results can also be compared to *Peter and Inan* [2007], who estimate a peak precipitated energy flux of $\sim 10^{-2} \text{ ergs cm}^{-2} \text{ s}^{-1}$ due to a 130 kA discharge. In Figure 2, the precipitated fluxes peak at $0.9 \times 10^{-3}, 1.5 \times 10^{-3}$, and $1.5 \times 10^{-3} \text{ ergs cm}^{-2} \text{ s}^{-1}$ for sources at $\lambda_m = 35^\circ, 45^\circ$, and 55° , respectively. This factor of 10 difference compared to *Peter and Inan* [2007] is due to differences in the source latitude and peak current; all other model parameters are identical.

This precipitated flux compares favorably to measurements by *Voss et al.* [1998] aboard the S81-1 satellite of a peak flux of $\sim 10^{-3} \text{ ergs cm}^{-2} \text{ s}^{-1}$. Unfortunately, to our knowledge, *Voss et al.* [1998] did not have a measurement of the causative lightning peak current.

[11] Following Monte Carlo calculations of energy deposition in the upper atmosphere, Figure 3 shows the altitude profiles of secondary ionization and optical emissions as a function of time, due to precipitation at $L = 2.5$. These results are for the same 100 kA discharge at a lightning source magnetic latitude of $\lambda_m = 35^\circ$, equivalent to the southern tip of Texas. We calculate optical emission rates for the first positive (1P), second positive (2P), and Vegard-Kaplan (V-K) band systems of N_2 ; the $\text{O}({}^1\text{S})$ and $\text{O}({}^1\text{D})$ metastable states of oxygen; the first negative (1N) and Meinel (M) band systems of N_2^+ ; and the first negative (1N) band system of O_2^+ .

[12] We note that the ionization profile and the emission rates for most of the band systems track each other, thanks to the short lifetimes and negligible quenching of these excited states. The peak of ionization, and the peak of these prompt emissions, occur at $\sim 80\text{--}90$ km altitude. The $\text{O}({}^1\text{D})$ emission, however, is orders of magnitude weaker at lower altitudes, but stronger at 250–300 km altitudes, due to its high quenching at lower altitudes (note the difference in color scale). Note that while the $\text{O}({}^1\text{D})$ emission is fully quenched at lower altitudes, the $\text{O}({}^1\text{S})$ emission is only weakly affected by quenching. Quenching effects can also be observed in the forbidden Vegard-Kaplan band. We also observe multiple ionization peaks in time, corresponding to the multiple magnetospheric reflections. When the simulation is extended to 20 s (not shown), we observe 4–5 strong precipitation peaks, although the number depends on the source latitude, and the first peak is typically an order of magnitude stronger, as is evident from Figure 3. These multiple peaks are a consequence of weak path-integrated Landau damping through the magnetospheric reflections. The absolute magnitude of this Landau damping depends on the distribution of ~ 1 keV fluxes, which is known statistically but has large variability on a case-by-base basis [*Bell et al.*, 2002]. Higher damping during a particular event will result in suppression of these subsequent precipitation peaks.

[13] It is further evident from Figure 3 that there are distinct precipitation peaks at different altitudes. The peaks at 80–90 km occur prior to the peaks at 150–250 km. This is consistent with lower-energy electrons, which take longer to reach the ionosphere, precipitating at higher altitudes.

[14] Similar results are found for L shells ranging from $L = 1.3$ to 5.5, although the peak is typically found in the range $2.5 < L < 3.5$. Consistent with prior results of LEP modeling and observations, precipitation occurs first at the lowest L shells, thanks to the shorter propagation distance, and moves toward higher L shells with time, so that the precipitation hot spot shifts poleward over the course of 2–3 s [e.g., *Johnson et al.*, 1999].

4. Camera and Photometer Signatures

[15] We apply a geometric algorithm, integrating through the 3D emitting volume (given in latitude, longitude, and altitude coordinates) from a specified ground location, to

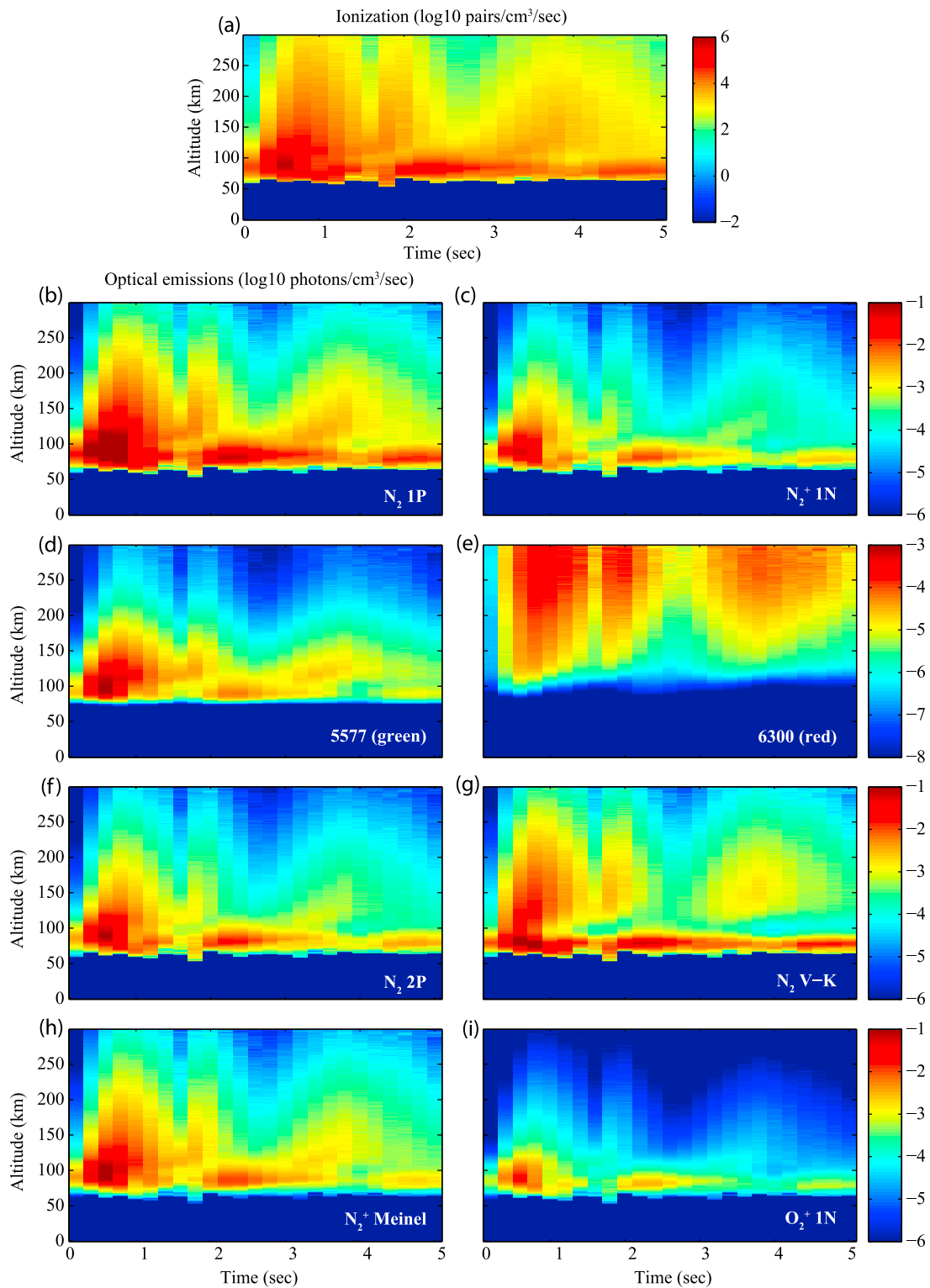


Figure 3. (a) Ionization and (b–i) optical emission rates calculated for $L = 2.5$, as a function of time and altitude, for a 100 kA discharge at $\lambda_m = 35^\circ$. Note that the color scales on each of the emission rate panels are identical, except for the $O(^1D)$ 6300 Å emission, whose color scale is enhanced by 2 orders of magnitude.

determine the brightness, in rayleighs, observed on the ground at each time step. Figure 4 shows results for the same 100 kA discharge at 35° magnetic latitude.

[16] Figure 4 (top left) shows the N_2 1P brightness, integrated in altitude, at $t = 1$ s; the color scale is logarithmic, from 10^{-5} (white) to 10^0 (red) R. The map shows the

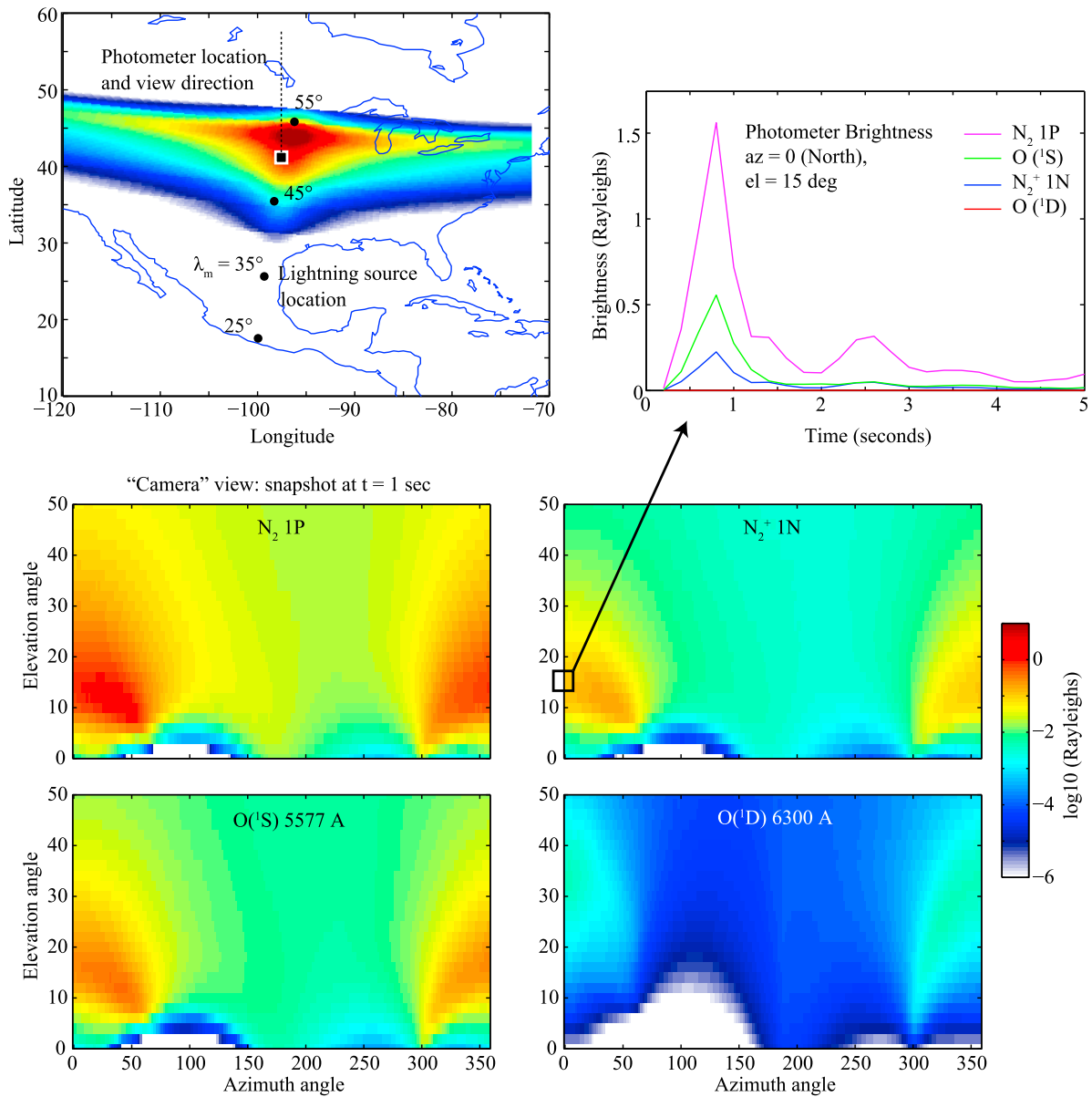


Figure 4. Results for 100 kA at $\lambda_m = 35^\circ$. (top left) Map showing precipitation region and lightning source locations for each magnetic latitude. (middle and bottom) Brightness in rayleighs, at $t = 1$ s, for the four emissions shown, covering nearly the entire “all-sky” view. This is the distribution over the sky that such a camera would see at this time. (top right) Photometer view, pointed north at 15° elevation, as a function of time, for the same four emissions.

lightning source location (including those for other simulations at different latitudes, described in section 5), and the camera and photometer locations, as they pertain to the panels below. The lower panels show “camera” views of these emissions at the same instant in time, for a camera placed at the location on the map. The camera views are nearly all-sky, though we have cut off the zenith portion in order to present the results as square images. Note that measurements with a real camera are not likely to be feasible, since the integration times required to see a few rayleighs would be longer than the ~ 1 s event; these views are simply shown to give an idea of the spatial distribution of

emissions. Figure 4 (top right) shows a “photometer” view, i.e., what a photometer with $10^\circ \times 10^\circ$ field of view would measure when pointed north, 15° above the horizon, as a function of time, for each of the four emissions mentioned earlier. Clearly, the N₂ 1P emission is the brightest, and the O(¹S) line is ~ 3 times weaker. The signatures show a distinct peak near ~ 1 s after the lightning discharge, consistent with the delay observed in subionospheric VLF detection of LEP. The O(¹D) line peaks at less than 0.01 R, and is too weak to warrant attention. The N₂⁺ 1N emission, which is dominated by the lines at 4278 \AA and 3914 \AA , will be adversely affected by atmospheric Rayleigh scattering (not

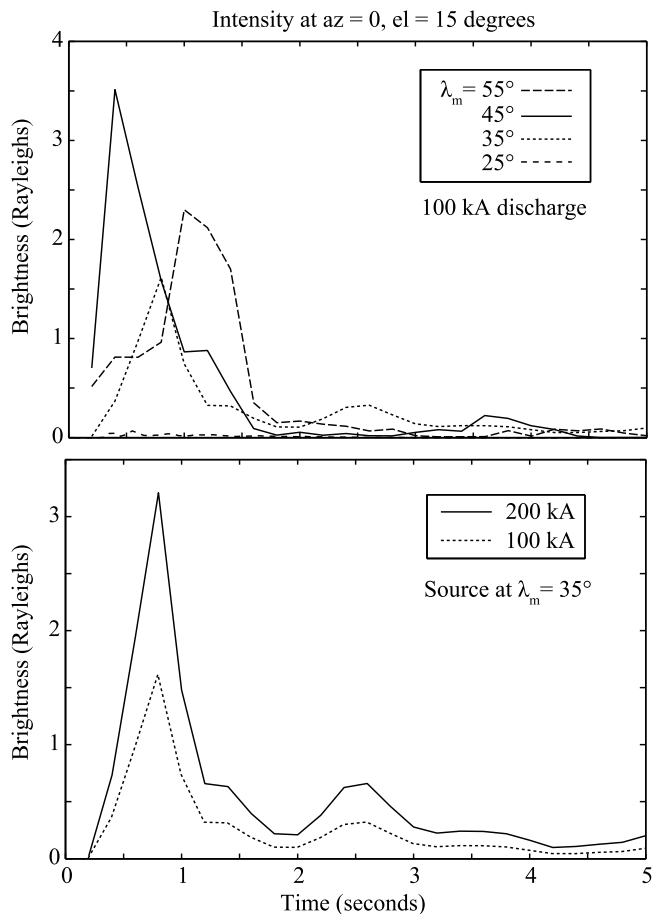


Figure 5. Photometer brightness curves for the N_2 1P emission with varying latitude and peak current. (top) Lightning source latitude variation, with 100 kA peak current. (bottom) Peak current variation, for lightning at $\lambda_m = 35^\circ$. Photometer location and viewing angle are the same as shown in Figure 4.

included in these calculations). Nonetheless, in section 6 we estimate the detectability of each of these emissions using a signal-to-noise ratio calculation.

[17] We should note here that the particular locations chosen for the camera and photometer, and the photometer viewing directions, were taken without thorough optimization. As such there are likely to be locations and viewing directions that are somewhat better in terms of total brightness. With a better located observing platform we have calculated a peak brightness of ~ 10 R in the N_2 1P emission, with corresponding increases in the other emissions.

5. Latitude and Peak Current Dependence

[18] Here we briefly investigate the dependence of the LEP optical signatures on lightning source location (latitude) and peak current. Figure 5 shows the photometric signatures for the N_2 1P emission for a range of source latitudes and for two peak currents. Figure 5 (top) shows that the strongest signatures are found for lightning at higher latitudes, $\lambda_m = 45^\circ$ and 55° . This is primarily due to the fact that at higher latitudes, the Earth's magnetic field is closer to

vertical, allowing more efficient coupling of the lightning EMP into the magnetosphere. At the lowest latitudes ($\lambda_m = 25^\circ$), the resulting emission signature has a peak of less than 0.1 R. For reference, along the magnetic meridian shown in Figure 4, $\lambda_m = 45^\circ$ and 55° correspond to Oklahoma and Minnesota, respectively, while $\lambda_m = 25^\circ$ is in the vicinity of Acapulco. Again, the location of the photometer on the ground has not been optimized; we estimate that the N_2 1P emission peaks at ~ 10 R for the 45° latitude source, for a more optimal ground observing location.

[19] Figure 5 (bottom) shows results for a 100 kA discharge (the same as shown previously) and a 200 kA discharge. Figure 5 (bottom) simply verifies what was stated earlier, that the emission brightness increases linearly with peak current, and this is expected from the model.

[20] While we have not investigated the effect of the pitch angle distribution here, *Marshall et al.* [2010] showed that a sine-shaped pitch angle distribution will reduce the precipitated flux, and thus optical brightness, by two orders of magnitude compared to the square pitch angle distribution. A more realistic pitch angle distribution that is not quite square will likely reduce the fluxes and brightness by a factor of 1–10.

6. Implications for Detectability

[21] *Marshall et al.* [2010] used a simple signal-to-noise ratio (SNR) calculation to determine the detectability of the optical signature of precipitation induced by VLF transmitters; here we conduct a similar calculation. We assume an $f/1.2$ optical system (a 75 mm diameter front aperture with a 10×10 degree field of view); a filter with 70% transmission; a Hamamatsu R5900U photomultiplier tube, which has a 16×16 mm active area with 17% peak quantum efficiency, 1 nA dark current, and 10^6 gain; and we filter the signal with 2 Hz bandwidth (yielding 0.25 s time resolution), which maintains the signal integrity shown in Figures 4 and 5.

[22] Each of the emissions will be added to a nighttime ambient background airglow, which we estimate from *Broadfoot and Kendall* [1968]. In the blue part of the spectrum, the natural airglow is dominated by O_2 Herzberg and Chamberlain bands, with a brightness of ~ 1 R/Å. For the $O(^1S)$ emission, we assume a typical background airglow of 250 R [*Chamberlain*, 1995] (which dominates over the ~ 1 R/Å background); for the $O(^1D)$ emission, the airglow reaches about 50 R. In the red and NIR region of the spectrum up to about 8000 Å, the background varies from about 1–5 R/Å, which is dominated by OH emissions. At their strongest in the optical spectrum, the OH (7-3) bands can reach up to 60 R/Å. Hence, a well-designed experiment will avoid the prominent OH emission regions.

[23] We use these background intensities to design a system of experiments for each of the eight emissions calculated here. The wavelength regions chosen are noted in Table 1, along with the fraction of the emitting system that falls in that band. These are used to calculate a total background intensity for typical airglow conditions, and in turn to calculate the SNR for an LEP event, where each of the emissions have been scaled to 5 R brightness in the N_2 1P system. Table 1 incorporates an approximate atmospheric transmission, calculated at the given wavelength at sea level

Table 1. Signal-to-Noise Ratios for Different Emissions, Assuming Brightnesses and Backgrounds Given for a 100 kA Discharge at $\lambda_m = 35^\circ$ ^{aa}

State	Brightness (R)	Wavelengths (Å)	Background (R/Å)	Airglow (R)	Atmospheric Transmission	SNR
N ₂ 1P	5.00	6500–7500	15	0	0.82	0.70
N ₂ 2P	1.19	3150–3450	1	0	0.25	0.54
N ₂ VK	4.46	2500–3500	1	0	0.05	2.05
N ₂ ⁺ M	1.82	7800–8800	2	5	0.82	0.15
N ₂ ⁺ 1N	0.74	4000–4300	15	0	0.50	0.57
O(¹ S)	1.25	5570–5585	3	250	0.64	4.27
O(¹ D)	0.006	6293–6308	10	50	0.70	0.02
O ₂ ⁺ 1N	0.22	5500–6500	10	0	0.67	0.03

^aEmissions are scaled to 5 R for N₂ 1P.

using MODTRAN5; the variable QE of the detector at each wavelength; the continuum background and airglow signal, as described above; and the fraction of the signal that passes through the fictional “filter”, as described by the wavelength regions in Table 1.

[24] Table 1 demonstrates that the O(¹S) emission line at 5577 Å is the most likely to be detected, with an SNR of ~4 for 1.25 R intensity. The band emissions calculated will be difficult to detect due to their broadband nature; the signal is spread out over a wide range in wavelength, to which will be added a significant background signal. Table 1 includes background contributions from the continuum and from OH emissions, as measured by *Broadfoot and Kendall* [1968]. For the O(¹S) emission, the primary contribution to the noise is the 250 R background airglow; hence, the SNR will increase or decrease linearly with the LEP signal brightness.

[25] The detectability of this small signal is supported by prior measurements using similar photometric devices. Recent (though unpublished) measurements at the HAARP heating facility in Alaska have been made with 1 R noise floor (T. Pedersen, private communication, 2010), and 1 R measurements of heater-induced airglow have been made [*Kendall et al.*, 2010], albeit of the 8446 Å line, which has far lower background.

[26] Emissions from LEP events should be easy to distinguish from other natural emissions (airglow and aurora due to geomagnetic activity, for instance). First, LEP events only occur at midlatitudes, so that aurora is unlikely to occur in the same region, except during intense geomagnetic activity. Second, the timing and location of these events is very closely tied to the lightning activity. For a lightning discharge at a given location and time (as reported by, for instance, the National Lightning Detection Network), the time delay and latitudinal offset are very well known, from previous observations and modeling of LEP events. Thus we expect time correlation between lightning discharges and optical observations, and the specific 1–2 s photometric profile shown in Figures 4 and 5, which will distinguish these events from natural fluctuations in the background airglow.

[27] Under the scenario that two large lightning discharges occur nearly simultaneously (within a few seconds of each other) in the same storm, it is possible that multiple events could occur in a short time span and overlap. We have analyzed the NLDN lightning data from two large storms on July 02 and July 04, 2000, that occurred over South Dakota and Nebraska, respectively [*Gerken and Inan*, 2004]. For the July 02 storm, NLDN reported over 37,000 lightning flashes in the time period from 03:00–09:00 UT. Of these,

329 flashes (0.9%) contained strokes over 100 kA (positive or negative), an average of one large stroke every ~3 min. Of these 329 flashes, 53 events, or 16%, occurred within 5 s of the previous one. The July 04 storm has very different characteristics: over 68,000 flashes were reported between 03:00–07:00 UT, but only 55 of those contained strokes over 100 kA, and only one of those occurred within 5 s of the one before it. Hence, it is reasonably likely that events will overlap in time, but these overlapping events will not be the majority.

7. Summary

[28] We present model calculations of optical emissions resulting from lightning-induced electron precipitation (LEP). We find that precipitated fluxes reach levels of $\sim 10^{-3}$ ergs cm⁻² s⁻¹ for a 100 kA discharge, consistent with satellite measurements by *Voss et al.* [1998]. These fluxes become considerably lower below 35° magnetic latitude. These fluxes result in optical emissions peaking at $\sim 10^{-1}$ photons cm⁻³ s⁻¹ in the N₂ 1P band system, and somewhat lower in other bands and lines. Viewed from the ground, these emissions can reach 10 R in N₂ 1P, or 3 R in O(¹S). By a simple SNR calculation, we show that this signal should be detectable from the ground.

[29] The largest source of uncertainty in this modeling scheme is the choice of pitch angle distribution in the radiation belts. *Marshall et al.* [2010] found that the square pitch angle distribution, used here, results in fluxes ~100 times higher than those of a sine-shaped pitch angle distribution. This would reduce the peak precipitated fluxes to 10^{-5} ergs cm⁻² s⁻¹. The more likely scenario is a pitch angle distribution somewhere between these two extremes. However, we note again that our fluxes are consistent with measurements by *Voss et al.* [1998], which supports the results of the present modeling study.

[30] **Acknowledgments.** R.A.M. was supported by NSF grant ATM-0724440 and an NSF CEDAR/GEM Postdoctoral Fellowship. J.B. would like to acknowledge support from NSF grant AGS-0840178. N.L. would like to acknowledge support from NSF grant ATM-0836326 and DARPA grant HR0011-10-1-0058-P00001.

[31] Robert Lysak thanks the reviewers for their assistance in evaluating this paper.

References

Baker, D. N., S. G. Kanekal, X. Li, S. P. Monk, J. Goldstein, and J. L. Burch (2004), An extreme distortion of the Van Allen belt arising from the “Halloween” solar storm in 2003, *Nature*, 432, 878–881.

- Bell, T. F. (1984), The nonlinear gyroresonance interaction between energetic electrons and coherent VLF waves propagating at an arbitrary angle with respect to the Earth's magnetic-field, *J. Geophys. Res.*, *89*(A2), 905–918.
- Bell, T. F., U. S. Inan, J. Bortnik, and J. D. Scudder (2002), The Landau damping of magnetospherically reflected whistlers within the plasmasphere, *Geophys. Res. Lett.*, *29*(15), 1733, doi:10.1029/2002GL014752.
- Bortnik, J. (2004), Precipitation of radiation belt electrons by lightning-generated magnetospherically reflecting whistler waves, Ph.D. thesis, Stanford Univ., Stanford, Calif.
- Bortnik, J., U. S. Inan, and T. F. Bell (2006a), Temporal signatures of radiation belt electron precipitation induced by lightning generated MR whistler waves: 1. Methodology, *J. Geophys. Res.*, *111*, A02204, doi:10.1029/2005JA011182.
- Bortnik, J., U. S. Inan, and T. F. Bell (2006b), Temporal signatures of radiation belt electron precipitation induced by lightning-generated MR whistler waves: 2. Global signatures, *J. Geophys. Res.*, *111*, A02205, doi:10.1029/2005JA011398.
- Broadfoot, A. L., and K. R. Kendall (1968), The airglow spectrum, 3100–10,000 Å, *J. Geophys. Res.*, *73*(1), 426–428.
- Chamberlain, J. W. (1995), *Physics of the Aurora and Airglow*, AGU, Washington, D. C.
- Gerken, E. A., and U. S. Inan (2004), Comparison of photometric measurements and charge moment estimations in two sprite-producing storms, *Geophys. Res. Lett.*, *31*, L03107, doi:10.1029/2003GL018751.
- Helliwell, R. A. (1965), *Whistlers and Related Ionospheric Phenomena*, Stanford Univ. Press, Stanford, Calif.
- Inan, U. S., and T. F. Bell (1977), The plasmopause as a VLF wave guide, *J. Geophys. Res.*, *82*(19), 2818–2827.
- Inan, U. S., S. A. Cummer, and R. A. Marshall (2010), A survey of ELF and VLF research on lightning-ionosphere interactions and causative discharges, *J. Geophys. Res.*, *115*, A00E36, doi:10.1029/2009JA014775.
- Johnson, M. P., U. S. Inan, and D. S. Lauben (1999), Subionospheric VLF signatures of oblique (nonducted) whistler-induced precipitation, *Geophys. Res. Lett.*, *26*(23), 3569–3572.
- Kendall, E., R. Marshall, R. T. Parris, A. Bhatt, A. Coster, T. Pedersen, P. Bernhardt, and C. Selcher (2010), Decameter structure in heater-induced airglow at the High Frequency Active Auroral Research Program facility, *J. Geophys. Res.*, *115*, A08306, doi:10.1029/2009JA015043.
- Lauben, D. S., U. S. Inan, and T. F. Bell (1999), Poleward-displaced electron precipitation from lightning-generated oblique whistlers, *Geophys. Res. Lett.*, *26*(16), 2633–2636.
- Lehtinen, N. G., U. S. Inan, and T. F. Bell (2001), Effects of thunderstorm-driven runaway electrons in the conjugate hemisphere: Purple sprites, ionization enhancements, and gamma rays, *J. Geophys. Res.*, *106*(A12), 28,841–28,856.
- Marshall, R. A., R. T. Newsome, N. G. Lehtinen, N. Lavassar, and U. S. Inan (2010), Optical signatures of radiation belt electron precipitation induced by ground-based VLF transmitters, *J. Geophys. Res.*, *115*, A08206, doi:10.1029/2010JA015394.
- Meredith, N. P., R. B. Horne, S. A. Glauert, D. N. Baker, S. G. Kanekal, and J. M. Albert (2009), Relativistic electron loss timescales in the slot region, *J. Geophys. Res.*, *114*, A03222, doi:10.1029/2008JA013889.
- Peter, W. B., and U. S. Inan (2007), A quantitative comparison of lightning-induced electron precipitation and VLF signal perturbations, *J. Geophys. Res.*, *112*, A12212, doi:10.1029/2006JA012165.
- Peter, W. B., M. W. Chevalier, and U. S. Inan (2006), Perturbations of mid-latitude subionospheric VLF signals associated with lower ionospheric disturbances during major geomagnetic storms, *J. Geophys. Res.*, *111*, A03301, doi:10.1029/2005JA011346.
- Rakov, V. A., and M. A. Uman (2003), *Lightning: Physics and Effects*, Cambridge Univ. Press, Cambridge, U. K.
- Rees, M. H. (1963), Auroral ionization and excitation by incident energetic electrons, *Planet. Space Sci.*, *11*(10), 1209–1218.
- Thorne, R. M., Y. Y. Shprits, N. P. Meredith, R. B. Horne, W. Li, and L. R. Lyons (2007), Refilling of the slot region between the inner and outer electron radiation belts during geomagnetic storms, *J. Geophys. Res.*, *112*, A06203, doi:10.1029/2006JA012176.
- Vallance Jones, A. (1974), *Aurora*, D. Reidel, Dordrecht, Netherlands.
- Voss, H. D., W. L. Imhof, M. Walt, J. Mobilia, E. E. Gaines, J. B. Reagan, and U. S. Inan (1984), Lightning induced electron precipitation, *Nature*, *312*, 740–742.
- Voss, H. D., M. Walt, W. L. Imhof, J. Mobilia, and U. S. Inan (1998), Satellite observations of lightning-induced electron precipitation, *J. Geophys. Res.*, *103*(A6), 11,725–11,744.

J. Bortnik, Department of Atmospheric and Oceanic Sciences, University of California, Rm. 7115, Math Sciences Bldg., Los Angeles, CA 90095, USA.

S. Chakrabarti, Center for Space Physics, Boston University, 725 Commonwealth Ave., Boston, MA 02115, USA.

N. Lehtinen and R. A. Marshall, STAR Laboratory, Stanford University, 350 Serra Mall, Stanford, CA 94305, USA. (ram80@stanford.edu)